Available online at www.sciencedirect.com
ScienceDirect
Trans. Nonferrous Met. Soc. China 34(2024) 3893−3904
Transactions of Nonferrous Metals Society of China
www.tnmsc.cn

Friction plug−riveting spot welding of AA 7075-T6 aluminum alloy and low carbon steel using 1045 steel rivet

Ya-jia LIU, Jian-yu LI, Ze-hao XIE, Shu-hai CHEN, Jian YANG, Ji-hua HUANG, Zhi-yi ZHAO

School of Materials Science and Engineering, University of Science and Technology Beijing, Beijing 100083, China

Received 18 April 2023; accepted 11 October 2023

Abstract: 7075-T6 aluminum alloy/low carbon steel joint was carried out via a novel friction plug−riveting spot welding process. This process utilized uniquely designed steel rivets with a tip and groove shape. The macro-morphology formation, microstructure, microhardness and lap shear performance of joints were investigated. As the spindle down distance increased, the rivet tip was friction welded with the lower steel sheet, resulting in the formation of a solid phase welding zone exhibiting metallurgical bonding. Additionally, a hook was formed in the joint, providing the mechanical locking. The results showed that under optimal parameters of spindle down distance of 3.4 mm, rotation speed of 4000 r/min, and spindle down speed of 2.4 mm/s, the lap shear load of the joints reached a maximum of 14.36 kN. Failure occurred at the aluminum alloy base metal.

Key words: friction plug-riveting spot welding; aluminum alloy; low carbon steel; dissimilar metal joining

1 Introduction

The evolution of automobile body materials is driven by the interplay among safety, economic considerations, and environmental policies, all of which aim to facilitate the design of lightweight car bodies [1]. The hybrid steel/aluminum car body design capitalizes on the strength and cost-effectiveness of steel [2], as well as the mass reduction and energy absorption capabilities of aluminum alloy [3,4]. Consequently, this design approach is extensively employed in automobile manufacturing.

It is worth noting that it is difficult to join steel and aluminum alloy due to its differing melting points and linear expansion coefficients [5,6]. Moreover, the formation of brittle Fe−Al intermetallic compounds (IMCs), such as Fe_2Al_5, $FeAl_2$, and $FeAl_3$ [7] can adversely affect joint performance [8,9]. As such, the joining of dissimilar metals like steel and aluminum remains a pressing issue in the field of welding.

The interfacial reaction can be efficiently regulated by introducing an interlayer at the steel−aluminum interface [10,11] or by applying coatings to the base metal (BM). Most of the relevant research had been conducted using the resistance spot welding (RSW) process. For instance, ZHANG et al [12] investigated the RSW of H220YD high-strength steel/AA6008-T6 dissimilar metal joints with a 4047 AlSi12 interlayer, and found that increasing thickness of the applied interlayer from 0 to 400 μm reduced the IMCs thickness from 4.0 to 0.6 μm. Similarly, ARGHAVANI et al [13] reported that the presence of Zn coatings on the low carbon steel resulted in a lower IMCs thickness at the steel−aluminum interface during the RSW process. IBRAHIM et al [14] employed an Al−Mg alloy interlayer to join AA6061-T6 and stainless steel

Corresponding author: Shu-hai CHEN, Tel: +86-10-62334859, E-mail: shchenhit@gmail.com;
Zhi-yi ZHAO, Tel: +86-10-82375294, E-mail: zhaozhiyi@263.net
DOI: 10.1016/S1003-6326(24)66646-X

using RSW, and found that Mg diffusion to the aluminum side inhibited Al−Fe bonding, thereby reducing the thickness of Fe−Al IMCs.

However, the application of RSW in the manufacturing of steel/aluminum car bodies has been constrained because of the poor welding spot surface quality, a propensity for defects and electrode burnout [15]. Therefore, scholars turned their attention to explore alternative welding methods such as self-piercing riveting (SPR) [16] and flow drill screw (FDS) [17]. However, SPR is not suitable for joining high-strength steel and aluminum alloy dissimilar metals [18], and FDS has a lengthy riveting process and high costs. Fortunately, recent advancements in solid-phase welding methods have mitigated the effects of property mismatches between dissimilar metals and ensured quality joint formation [19]. Consequently, most current research primarily seeks to enhance existing solid-phase welding methods and proposes a hybrid mechanical−metallurgical joining process to circumvent issues caused by IMCs in dissimilar metals joining. For example, MENG et al [20] proposed a state-of-the-art hybrid mechanical−metallurgical welding method called friction-based welding techniques to join metal and polymer heterojunctions, which improved mechanical interlocking through a rational tool design. NIU et al [21] used a resistance rivet welding (RRW) method to join AA6061-T6 and press hardened steel, achieving a maximum lap shear load of 4.9 kN. MILES et al [22,23] proposed the friction bit joining (FBJ) process to join DP 980 steel and AA5754 owing to the low heat input advantages of the friction welding process. They measured a maximum lap shear load of 6.4 kN of joint with FBJ, which was 1.4 kN higher than that with SPR. SHAN et al [24] used the friction stir riveting (FSR) method to join AA6061-T6 and DP 600 steel, resulting in the highest average tensile-shear strength of 300 MPa for joints without aluminum inclusions. In addition, welding methods such as resistance element welding (REW) [25] and friction element welding (FEW) [26] with maximum tensile−shear loads of 6.074 and 10.6 kN of joints, respectively, had also been used to join steel/aluminum dissimilar metals.

Despite the valuable insights provided by previous research, a comprehensive understanding of how each parameter influences joint performance remains elusive. This paper developed a novel friction plug-riveting spot welding process to join AA7075-T6 and low carbon steel. To mitigate the formation of IMCs, which is more prevalent in dissimilar metals, a steel rivet was introduced into the welding process. Taking into account its machinability and heat treatment characteristics, the medium carbon steel (1045) was selected as the rivet BM. The rivet was designed with a groove to accommodate the extruded aluminum alloy and featured a tip at the bottom for drilling through the aluminum sheet. The macro-morphology formation, microstructure, microhardness and lap shear performance of joints were investigated using the optimized parameters. The friction plug-riveting spot welding method proposed in this work provides technical support for the steel/aluminum lightweight composite car manufacturing and has strong theoretical and academic value on the research on the metallurgical connection control mechanism of the circumferential friction interface.

2 Experimental

2.1 Materials

The base materials utilized in this study were 2 mm-thick AA7075-T6 sheets and 2 mm-thick low carbon steel sheets, both with dimensions of 125 mm × 39 mm. Considering the machinability and heat treatment characteristics required for the rivet in the experiment, the medium carbon steel (1045) was chosen as the rivet BM. The superior cutting performance of 1045 steel facilitated the drilling of the welded sheets. The tensile strength of AA7075-T6 and 1045 rivets were 524 and 600 MPa respectively, and the yield strength of low carbon steel was 235 MPa. The hardness values of the low carbon steel and 1045 rivet utilized in this study were approximately HV 160 and HV 320, respectively. The element components of the sheets and rivet are summarized in Table 1 [27,28,29].

2.2 Friction plug−riveting spot welding experiment method

The machine specifically developed for the friction plug−riveting spot welding process is shown in Fig. 1. A dual servo motors system was designed for rotation (0−5000 r/min) and downward movement (0−10 mm/s) of the rivet. A close-up view of the welding platform, including the pressure

Table 1 Element components of AA7075-T6, low carbon steel and 1045 steel

Material	Content/wt.%								
AA7075-T6	Si	Mn	Fe	Cu	Mg	Cr	Zn	Ti	Al
	≤0.4	≤0.3	≤0.5	1.2−2.0	2.1−2.9	0.18−0.28	5.1−6.1	≤ 0.2	Bal.
Low carbon steel	C		Si	Mn		S	P		Fe
	0.14−0.22		≤0.3	0.3−0.65		≤0.045	≤0.045		Bal.
1045 steel	Cu	Cr	Ni	C	Mn	Si	S	P	Fe
	≤0.25	≤0.25	≤0.25	0.43−0.5	0.6−0.9	0.17−0.37	≤0.035	≤0.035	Bal.

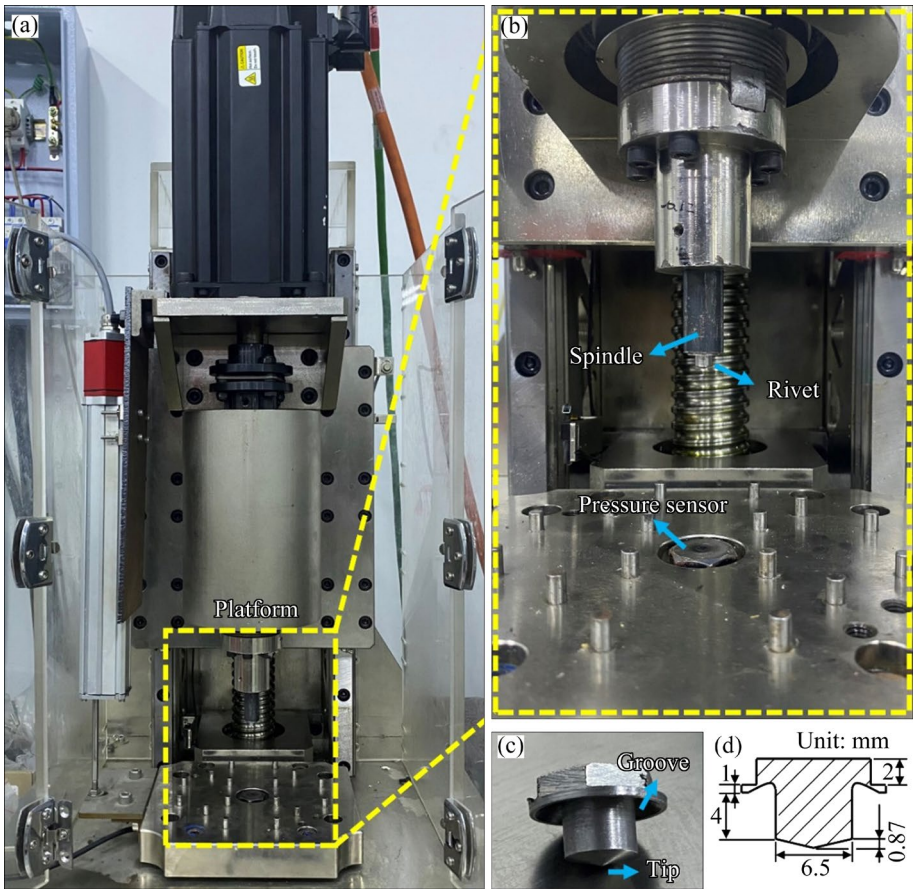

Fig. 1 Welding machine used for friction plug−riveting spot welding: (a) Overall view; (b) Close-up view of welding platform; (c, d) Rivet

sensor and rivet, is provided in Fig. 1(b). The bottom of the spindle has a hexagonal groove structure that matches the hexagonal size of the rivet head, ensuring a tight magnetic attachment of the rivet in the groove. Figures 1(c) and (d) present schematics of the rivet, which is designed with a groove and sharp tip to rapidly trap extruded aluminum alloy and drill through aluminum sheets.

Prior to the welding test, the rivet descends until its tip contacts the upper aluminum alloy sheet, facilitated by the automatic zero finding feature of the welding machine. Figure 2 outlines the detailed procedure of friction plug−riveting welding, which mainly contains three stages.

(1) Drilling stage: the rivet rotates at a speed of 2500 r/min and drills towards the aluminum sheet at a downward speed of 1.8 mm/s until its tip contacts the upper surface of the low carbon steel sheet (Fig. 2(a)).

(2) Welding stage: the rivet keeps rotating and feeds into the steel, creating lots of frictional heat to establish metallurgical bonding with the steel sheet. Meanwhile, the squeezed aluminum fills the rivet groove. Finally, an ensemble of aluminum alloy,

rivet and steel sheet is formed (Fig. 2(b)).

(3) Retreating stage: the spindle stops rotating rapidly and separates from the rivet. So far, the welding process is finished (Fig. 2(c)).

The friction plug−riveting spot welding process is affected by three key parameters, including spindle down distance, rotation speed and spindle down speed. During the entire welding process, the drilling stage maintained a parameter combination of a 2.0 mm spindle down distance, a 2500 r/min rotation speed and a 1.8 mm/s spindle down speed. However, the parameter combination for the welding stage was adjusted to achieve the welding process. The orthogonal experiments with three factors and three levels (L9(3^3)) were employed, and the average lap shear load of three samples under identical parameters was used for quality evaluation. Based on the orthogonal experiment results, the optimal parameter combination of a 3.4 mm spindle down distance, a 4000 r/min rotation speed and a 2.4 mm/s spindle down speed was set as the object of this study.

2.3 Characterization and mechanical testing

Metallographic samples were prepared by taking the center of joints to conduct wire cutting, and then were mechanically polished with diamond polishing pastes after polishing with 240#, 400#, 800#, 1000#, 1200#, 1500# and 2000# sandpaper. The steel and aluminum alloy were etched with 4 vol.% nitric acid and Keller reagent, respectively. The macro- and micro-structures were observed using a Zeiss optical microscope (OM) and a QUANTA 250 scanning electron microscope (SEM) equipped with energy disperse spectroscopy (EDS).

Lap shear tests of the samples were carried out on an Instron crew-test frame (1 mm/min). The average value of three samples under identical parameters was used to determine the final result. Figure 3 shows the location and dimensions of the lap shear test samples. The rivet is centrally located in the lap area, which is 39 mm × 39 mm. A 2 mm-thick spacer was used to make sure that the central axis of the sample and the tensile axis were aligned. With a load of 200 g and a holding time of 15 s, an HVS-1000TM/LCD microhardness tester was employed to assess the microhardness in various regions of the typical joint.

3 Results and discussion

3.1 Evolution of joint morphology

Figure 4 illustrates the evolution of joint morphology under different spindle down distances

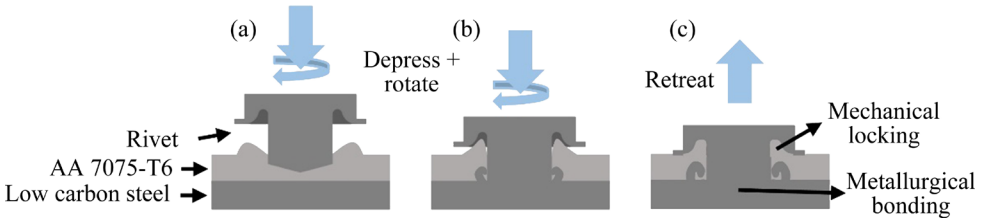

Fig. 2 Schematic illustrations of friction plug−riveting spot welding: (a) Drilling stage; (b) Welding stage; (c) Retreating stage

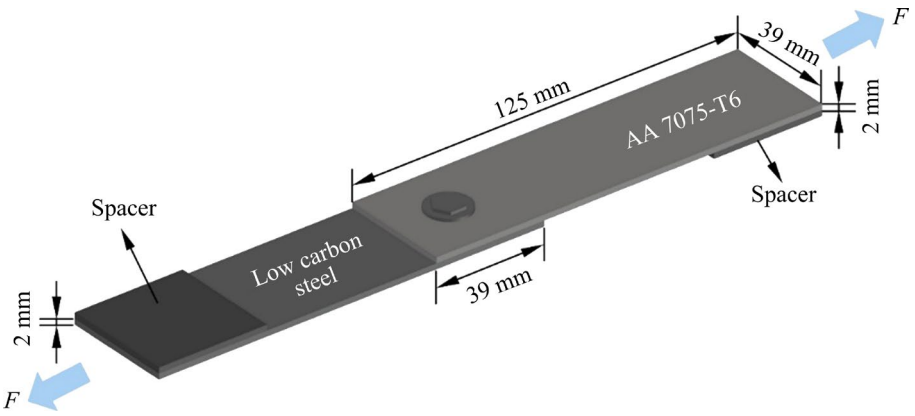

Fig. 3 Schematic diagram of lap shear testing

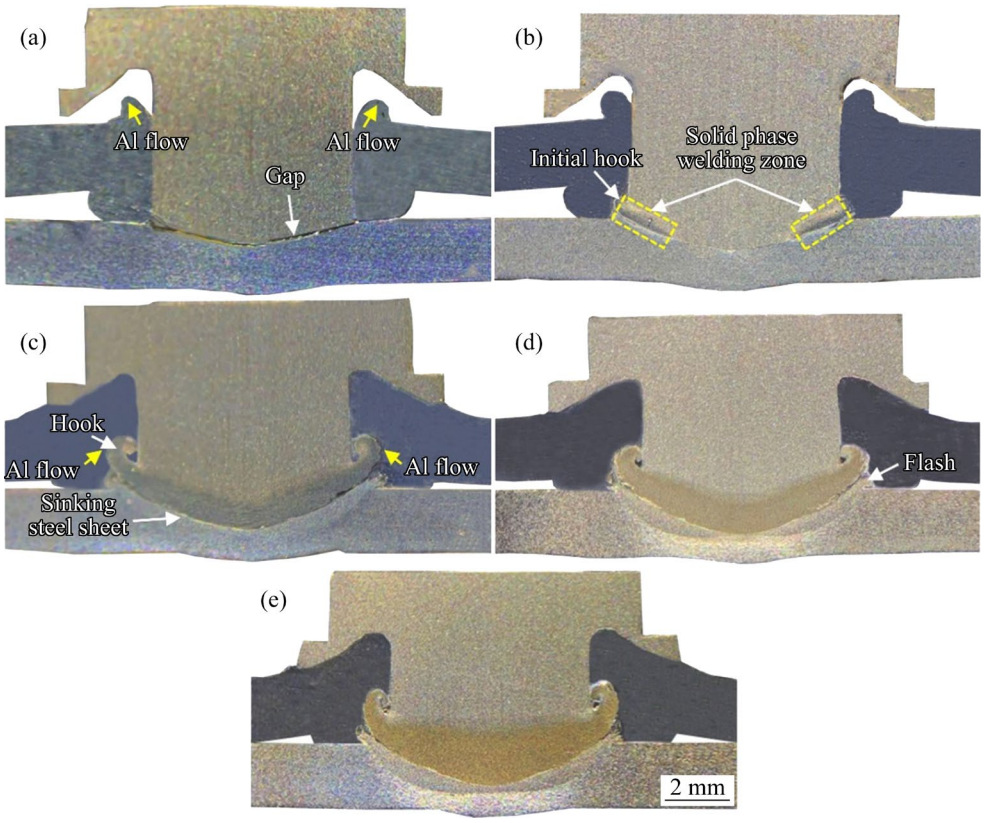

Fig. 4 Evolution of joint morphology under different spindle down distance: (a) 2.6 mm; (b) 2.8 mm; (c) 3.0 mm; (d) 3.2 mm; (e) 3.4 mm

using the optimal parameter combination of a spindle down distance of 3.4 mm, a rotation speed of 4000 r/min and a spindle down speed of 2.4 mm/s. The rivet had drilled through the upper aluminum alloy at this moment. During the drilling stage, aluminum was extruded and gradually flowed to the rivet groove, leaving a large gap between the rivet cap and the steel sheet. At the welding stage, when the spindle down distance was 2.6 mm, a gap persisted between the rivet and the steel sheet, indicating insufficient metallurgical bonding, as shown in Fig. 4(a). Subsequently, the rivet tip was consumed to form a solid-phase welding zone, which initially appeared as a small region at the rivet ends when the spindle down distance was 2.8 mm. Besides, the initial hook resulted from the rivet tip flowing along the sheet length direction under pressure, as shown in Fig. 4(b). With the spindle down distance further increased to 3.0 mm, an obvious solid-phase welding zone formed. At the same time, extruded aluminum alloy filled the rivet groove, as shown in Fig. 4(c). On the one hand, the low carbon steel sheet deformed during the welding process because its hardness and yield strength were lower than the 1045 steel rivet, causing the rivet tip to flow diagonally upward along the deforming steel sheet. On the other hand, due to the inward resistance from aluminum flow, the extruded rivet rolled inward, leading to a hook formation. Furthermore, the rivet cap was tightly positioned on top of the aluminum sheet. The gap between the rivet groove and aluminum sheet gradually disappeared at a spindle down distance of 3.4 mm, as shown in Figs. 4(d, e). Concurrently, the solid-phase welding zone expanded and the hook became more visible.

It was noteworthy that the hook became more incurvate as the rivet descended during the welding process. At the initial welding stage, the rivet tip became soft rapidly and was crushed firstly due to the high temperature at the rivet tip and the high thermoplastic of the rivet, as shown in Fig. 5(a). Subsequently, at the medium welding stage, the lower steel sheet depressed because of its lower microhardness and yield strength compared to the 1045 rivet, as shown in Fig. 5(b). The depression of the lower steel sheet caused the crushed rivet to flow in the direction of the depression. Furthermore,

as the rivet continued to descend, the aluminum around the rivet applied inward resistance to inhibit the flow of the crushed rivet, leading to the formation of the hook, as shown in Fig. 5(c). The hook has the ability to realize mechanical interlocking, making the mechanical performance of joints further favor when the joints are under the lap shear load in the experiment.

3.2 Microstructure

During the friction plug−riveting spot welding process, the stirring effect and friction heat production from the rivet caused various regions of the joint to undergo diverse thermal cycling and plastic deformation processes. At last, the different grain characteristics appeared in the different regions.

Figure 4(e) demonstrates an ensemble of the aluminum alloy, low carbon steel and the rivet. Figure 6 displays the microstructure of different regions of the joint under optimal parameters, which can be mainly divided into six typical zones.

The rivet BM (Region I) was made up of ferrite and pearlite, as shown in Fig. 6(b). The rivet HAZ_1 (Region II) that included a mixture of ferrite, pearlite and martensite shown in Fig. 6(c), was located near the rivet BM in a low temperature area. The low temperature caused some pearlites to austenitize and eventually transform into coarse martensite due to the high cooling rate. The rivet HAZ_2 (Region III) shown in Fig. 6(d) is close to the strongest welding zone. The temperature of the rivet HAZ_2 was between Ac_3 (the threshold temperature at which ferrite is fully transformed into austenite) and Ac_1 (the threshold temperature at which ferrite is fully transformed into austenite), leading to partial austenitization and consequently the formation of a mixed phase of ferrite and coarse martensite. The

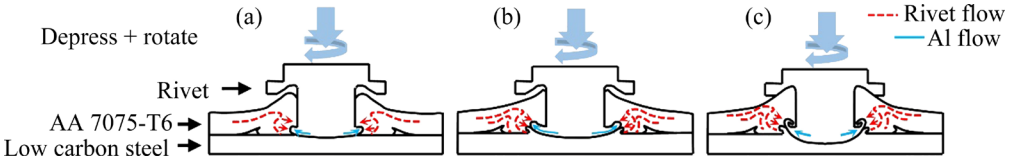

Fig. 5 Process of hook formation at welding stage: (a) Initial stage; (b) Medium stage; (c) Late stage

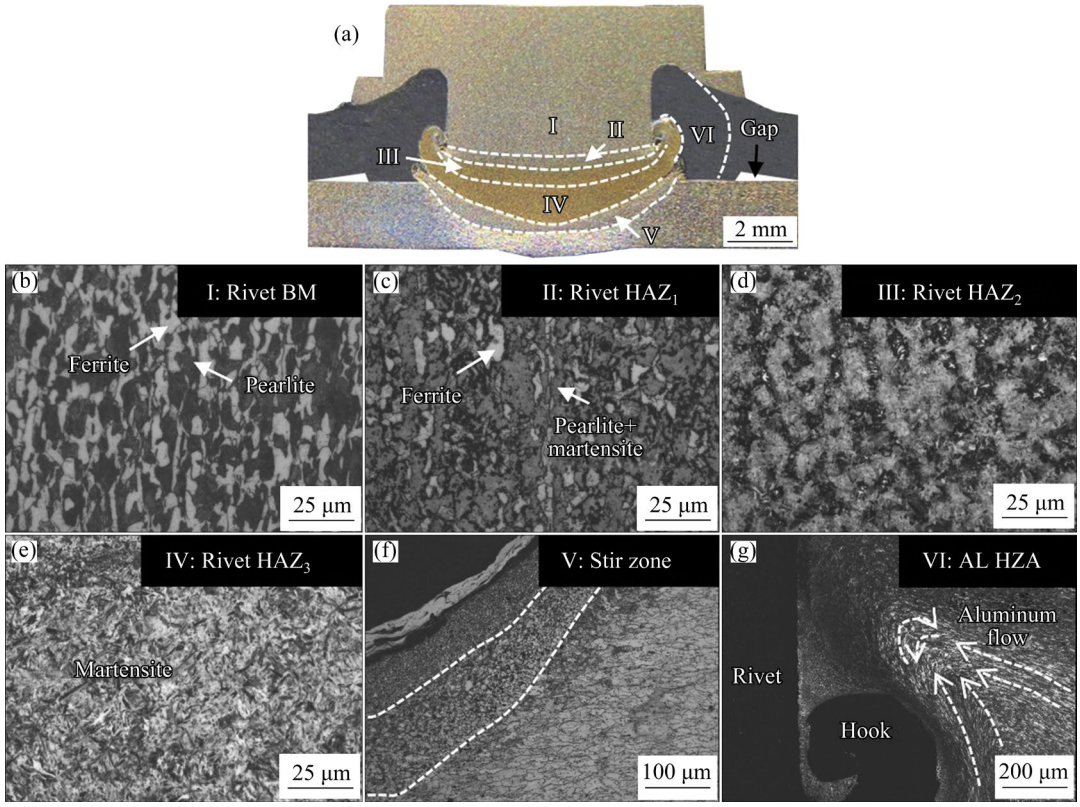

Fig. 6 Macro-morphology and microstructure of welding joint: (a) Macro-morphology; (b) Rivet BM; (c) Rivet HAZ_1; (d) Rivet HAZ_2; (e) Rivet HAZ_3; (f) Stir zone; (g) Al HAZ

rivet HAZ_3 (Region IV) in Fig. 6(e) displays an ultrafine martensite structure that experiences strong friction and high temperature. The peak temperature of the rivet HAZ_3 exceeded Ac_3, causing the grains to turn into martensite after complete austenitization and rapid cooling. Due to the temperature effect and the high-speed rotation of the rivet, numerous dislocations and slips occurred at the rivet and the steel sheet interface. This provided a location and energy for grain nucleation, resulting in a large number of equiaxed fine grains in the stir zone (Region V), as shown in Fig. 6(f). However, in the area of the steel sheet slightly away from the rivet and the steel sheet interface, dynamic recrystallization degree and grain refinement were lower than that at the interface due to better heat dissipation. As a result, new fine grains without distortion formed. Additionally, grains close to the steel sheet BM in the stir zone were stretched horizontally after extrusion by the rivet. Due to squeezing by the hook and rotational friction around the rivet, the flow behavior of aluminum alloy occurred in the direction indicated by the arrows in Region VI, as shown in Fig. 6(g). The grains in the Al HAZ close to the rivet underwent dynamic recrystallization under high temperature and plastic deformation impact. Meanwhile, due to high rotation by the rivet, grains were broken into fine grains even if they grew.

SEM and EDS were utilized to further investigate the microstructure of the joint. The SEM images and EDS line scanning are shown in Fig. 7. Table 2 lists the EDS point scanning results of different locations in Fig. 7. The entire morphology

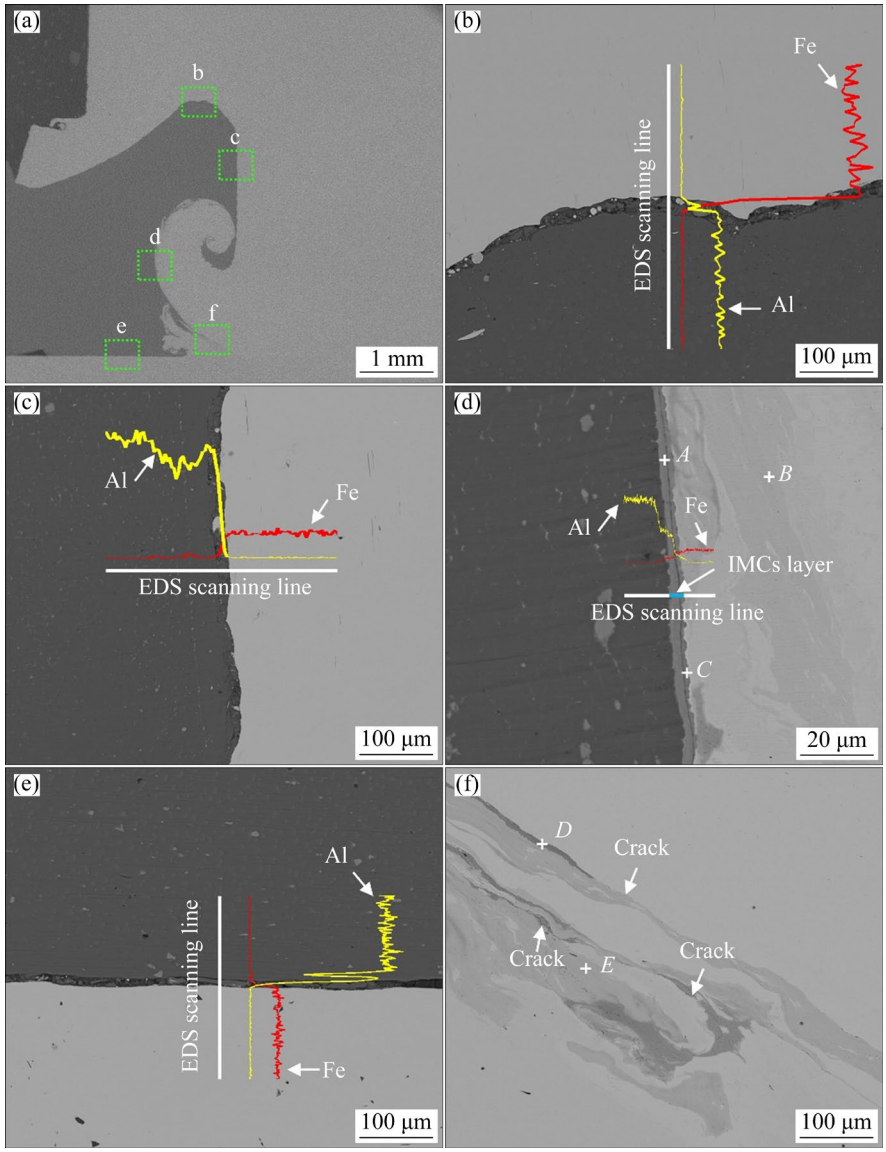

Fig. 7 SEM images of left side of cross-section of welded joint

Table 2 EDS point scanning results (at.%)

Point in Fig. 7	Fe	Al
A	22.19	77.81
B	81.26	18.74
C	34.41	65.59
D	26.18	73.82
E	73.07	26.93

of the left side cross-section of the joint is shown in Fig. 7(a). The EDS line scanning results in Figs. 7(b, c) showed that there was a gap between the rivet cap and aluminum sheet, confirming that Al did not diffuse into the rivet. This phenomenon was attributed to the rivet cap being minimally affected by heat. Figure 7(d) shows the hook and aluminum interface. The EDS line scanning result indicated a 2 μm-thick IMCs layer composed of $FeAl_3$ and $FeAl_2$. The formation of IMCs was due to the extremely high temperature in this region and vigorous aluminum flow caused by severe rotation of the rivet. Consequently, Al diffused into the rivet hook, leading to a metallurgical reaction between Fe and Al. The gap between the aluminum sheet and steel sheet was filled with fragmental steel and aluminum, as shown in Fig. 7(e). The high temperature around the rivet tip and steel sheet interface, coupled with strong flowability of aluminum, resulted in Fe−Al compound formation, as shown in Fig. 7(f). The cracks in Fig. 7(f) were caused by a sudden temperature drop at the end of the welding process. Therefore, this part of the IMCs should be avoided as it significantly impacts joint performance.

3.3 Microhardness

Figure 8 illustrates the microhardness distribution of the welded joint. The microhardnesses of the rivet BM, steel BM and aluminum BM were HV 320, HV 160 and HV 133, respectively. As depicted in Fig. 8(a), the microhardness of the rivet HAZ initially increased and then stabilized as the heat generated from rotating friction changed. As analyzed in Section 3.2, partial austenitization of grains occurred in the rivet HAZ_{1+2}. The closer to the lower side of the rivet HAZ, the stronger the rotational friction, resulting in greater austenitization. Eventually, pearlite transformed into martensite after rapid cooling,

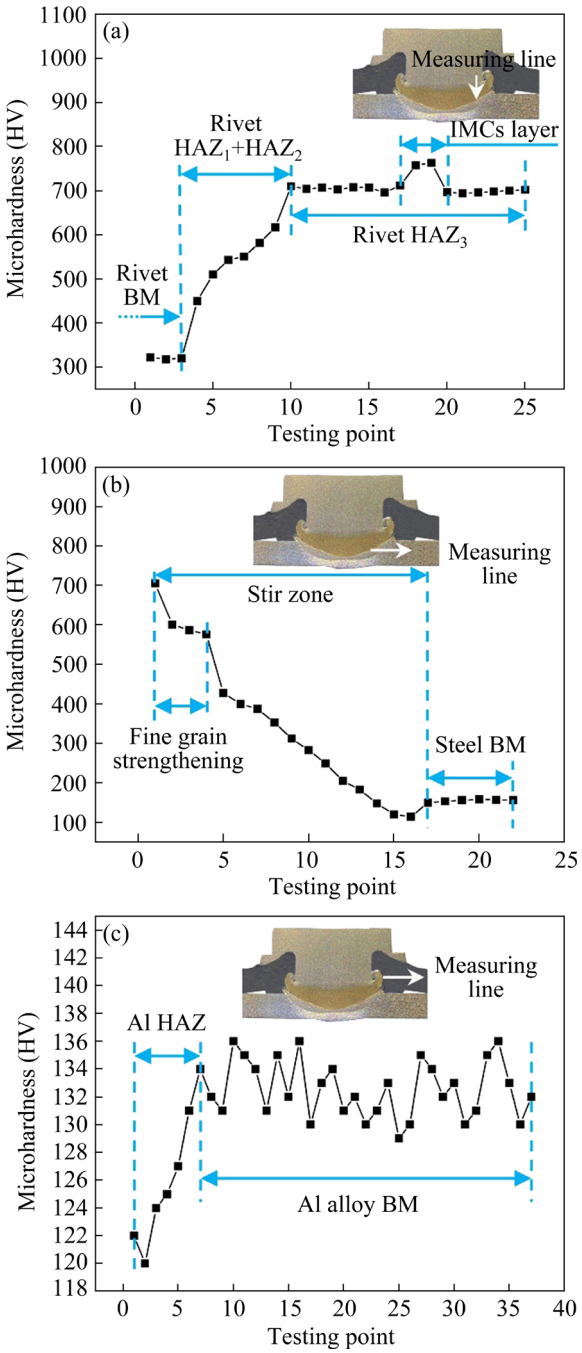

Fig. 8 Microhardness distribution of welded joint: (a) Rivet side; (b) Steel side; (c) Al alloy side

causing an increase in microhardness. The complete austenitization of grains took place in the rivet HAZ_3, where the microhardness reached about HV 720 due to the ultrafine martensite structure. It was noteworthy that a peak microhardness occurred in the rivet HAZ_3 as a result of the formation of a brittle-hard Fe−Al IMCs layer. The rivet failure mode tended to take place in this IMCs area and expanded along the IMCs layer. Figure 8(b) presents the microhardness of the steel sheet side.

As mentioned in Section 3.2, grain sizes varied in different areas away from the rivet and the steel sheet interface. The closer to this interface, the finer the grain. The fine grain strengthening occurred near the rivet due to high-speed rotation and stirring by the rivet, resulting in maximum microhardness. As measurements proceeded, the microhardness of the stir zone softened due to low temperature away from the rivet and the steel sheet interface during welding, finally recovering to steel BM hardness level. As shown in Fig. 8(c), the hardness of the Al HAZ decreased with increasing temperature, and the hardness of the aluminum sheet side recovered from rivet outward to Al BM hardness level.

3.4 Mechanical performance

The joint strength primarily originated from the bonding interface between the rivet and the lower steel sheet. The lap shear load at different spindle down distance (rotation speed = 4000 r/min, spindle down speed = 2.4 mm/s), spindle down speed (spindle down distance = 3.4 mm, rotation speed = 4000 r/min) and rotation speed (spindle down distance = 3.4 mm, spindle down speed = 2.4 mm/s) were measured by a variable-controlling approach based on the optimal parameter combination. The average lap shear load value of three samples was taken as the final result, as shown in Fig. 9. The test revealed that as the spindle down distance increased, the lap shear load also increased due to the growth of the solid-phase welding zone (Fig. 4). When the spindle down distance was 3.4 mm, the lap shear load reached 14.36 kN. In general, for samples with constant spindle down distance and rotation speed, the lap shear load increased as the spindle down speed increased. It was worth noting that when the spindle down speed was 1.2 mm/s, the lap shear load was the lowest. This issue primarily arose due to the short welding time and minimal downward pressure leading to weak metallurgical bonding. When the spindle down speed and the spindle down distance were held constant, a low or high rotation speed resulted in a low lap shear load on the joint. The reason was that, at a low rotation speed, the heat produced by rotating friction was insufficient to realize strong metallurgical bonding. However, at a high rotation speed, excessive heat built up inside the joint promoted the Al diffusion and fostered the development of brittle IMCs.

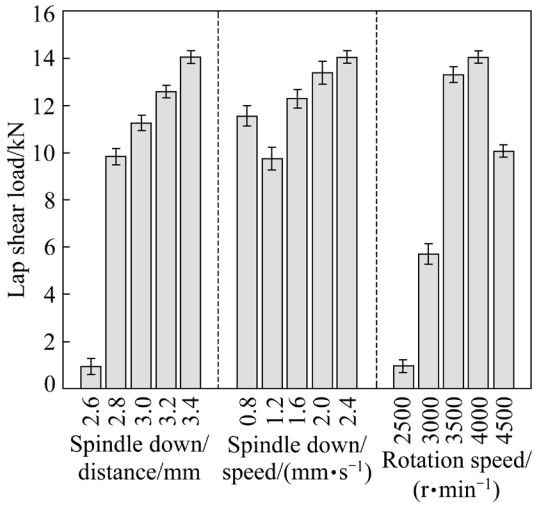

Fig. 9 Results of lap shear test under different spindle down distance, spindle down speed and rotation speed

Figure 10 shows the failure modes of different samples after the lap shear test, which were divided into interface failure, rivet failure and Al BM failure. In the case of interface failure, the rivet and steel sheet separated along the bonding interface due to insufficient metallurgical bonding between them, as shown in Fig. 10(a). The enlarged view of the fracture on the steel sheet side, shown in Fig. 10(d), reveals the marks of rotating friction from the rivet on the steel sheet. As for the rivet failure mode shown in Figs. 10(b, e), a portion of the fracture displayed a river pattern, which was a typical brittle fracture characteristic, indicating the presence of brittle IMCs (Fig. 10(f)). Additionally, fine dimples, indicative of plastic fracture characteristic, were also present, as shown in Fig. 10(g). With regard to the Al BM failure mode shown in Fig. 10(c), the fracture took place in the Al BM. The joints exhibiting this failure mode possess strong load-carrying capacity.

4 Conclusions

(1) In the friction plug−riveting spot welding process, the metallurgical bonding between the rivet and the steel sheet was achieved through high-speed rotational friction of the rivet. With the increase of the spindle down distance, the rivet was consumed to bond the steel sheet. When the spindle down distance reached 3.4 mm, the metallurgical bonding between the rivet and the steel sheet was the most, resulting in optimal mechanical performance.

(2) The hook formed in the joint enabled

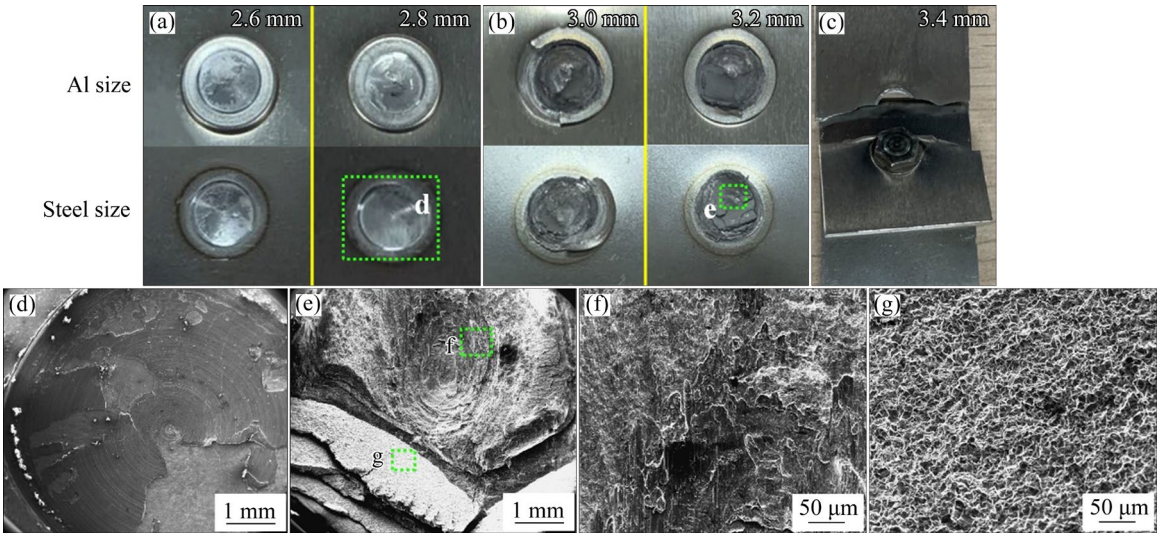

Fig. 10 Images of fracture surface after lap shear test: (a) Macro-morphology of interface failure; (b) Macro-morphology of rivet failure; (c) Macro-morphology of Al BM failure; (d, e) Enlarged view of fracture surface; (f, g) Typical fracture morphologies marked in (e)

mechanical interlocking, enhancing the mechanical performance of joints under lap shear load in the experiment.

(3) Six typical regions were formed in the joint: rivet BM, rivet HAZ_1, rivet HAZ_2, rivet HAZ_3, stir zone and Al HAZ. The interface between rivet and the steel sheet, such as rivet HAZ_3 and upper stir zone, experienced the strongest friction and the highest temperature. The grain near this interface transformed into ultrafine martensite after rapid cooling, resulting in a maximum microhardness of HV 720.

(4) The joint with Al BM failure mode exhibited the highest lap shear load of 14.36 kN under a parameter combination of 3.4 mm spindle down distance, 4000 r/min rotation speed and 2.4 mm/s spindle down speed.

CRediT authorship contribution statement

Ya-jia LIU: Conceptualization, Investigation, Data curation, Writing − Original draft; **Jian-yu LI:** Investigation, Validation; **Ze-hao XIE:** Visualization; **Shu-hai CHEN:** Resources, Writing − Review & editing, Supervision; **Jian YANG** and **Ji-hua HUANG:** Formal analysis; **Zhi-yi ZHAO:** Writing − Review & editing.

Declaration of competing interest

The authors declare that they have no known competing financial interests or personal relationships that could have appeared to influence the work reported in this paper.

Acknowledgments

This work was financially supported by the National Natural Science Foundation of China (No. 51875037).

References

[1] XIONG Feng, WANG Deng-feng, MA Zheng-dong, CHEN Shu-ming, LV Tian-tong, LU Fang. Structure-material integrated multi-objective lightweight design of the front end structure of automobile body [J]. Structural and Multidisciplinary Optimization, 2018, 57(2): 829−847.

[2] PERKA A K, JOHN M, KURUVERI U B, MENEZES P L. Advanced high-strength steels for automotive applications: Arc and laser welding process, properties, and challenges [J]. Metals, 2022, 12(6): 1051−1051.

[3] KACZYŃSKI P, SKWARSKI M, JAŚKIEWICZ K. Development of the technology for press-forming of energy-absorbing elements made of 7075 aluminum alloy [J]. Journal of Manufacturing Processes, 2020, 50(C): 676−683.

[4] SARAVANAN S, RAGHUKANDAN K. Microstructure, strength and welding window of aluminum alloy−stainless steel explosive cladding with different interlayers [J]. Transactions of Nonferrous Metals Society of China, 2022, 32(1): 91−103.

[5] YANG Jin, OLIVEIRA J P, LI Yu-long, TAN Cai-wang, GAO Chen-kai, ZHAO Yi-xuan, YU Zhi-shui. Laser techniques for dissimilar joining of aluminum alloys to steels: A critical review [J]. Journal of Materials Processing Technology, 2022, 301: 117443.

[6] LI Zhong-tao, MA Shi-hua, ZHAO Shi-jun, ZHANG Wei-dong, PENG Fei, LI Qian, YANG Tao, WU Chia-Yi, WEI Dai-xiu, CHOU Yi-Chia, LIAW P K, GAO Yan-fei, WU Zheng-gang. Achieving superb strength in single-phase FCC alloys via maximizing volume misfit [J]. Materials

Today, 2023, 63:108−119.

[7] LIU Gui-qian, GAO Xiang-dong, PENG Cong, LIU Xiu-hang, HUANG Yi-jie, ZHANG Yan-xi, YOU De-yong. Tensile resistance, microstructures of intermetallic compounds, and fracture modes of welded steel/aluminum joints produced using laser lap welding [J]. Transactions of Nonferrous Metals Society of China, 2020, 30(10): 2639−2649.

[8] MATSUDA T, HATANO R, OGURA T, SUZUKI R, SHOJI H, SANO T, OHATA M, HIROSE A. Effect of mismatch in mechanical properties on interfacial strength of aluminum alloy/steel dissimilar joints [J]. Materials Science & Engineering A, 2020, 786(C): 139437.

[9] DU Ming, WANG Wen-quan, ZHANG Xin-ge, NIU Jia-fei. Effect of process parameters on performances of TWIP steel/Al alloy dissimilar metals butt joints by laser offset welding [J]. Materials Science & Engineering A, 2022, 853: 143746.

[10] ZOU Tian-peng, YU Gao-yang, CHEN Shu-hai, HUANG Ji-hua, YANG Jian, ZHAO Zhi-yi, RONG Ji-ping, YANG Jin. Effect of Si content on interfacial reaction and properties between solid steel and liquid aluminum [J]. Transactions of Nonferrous Metals Society of China, 2021, 31(9): 2570−2584.

[11] CAO Xue-long, WANG Gang, XING Chang, TAN Cai-wang, JIANG Jun-jun. Effect of process parameters on microstructure and properties of laser welded joints of aluminum/steel with Ni/Cu interlayer [J]. Transactions of Nonferrous Metals Society of China, 2021, 31(8): 2277−2286.

[12] ZHANG Wei-hua, SUN Da-qian, HAN Li-jun, LIU Dong-yang. Interfacial microstructure and mechanical property of resistance spot welded joint of high strength steel and aluminium alloy with 4047 AlSi12 interlayer [J]. Materials & Design, 2014, 57: 186−194.

[13] ARGHAVANI M R, MOVAHEDI M, KOKABI A H. Role of zinc layer in resistance spot welding of aluminium to steel [J]. Materials & Design, 2016, 102: 106−114.

[14] IBRAHIM I, ITO R, KAKIUCHI T, UEMATSU Y, YUN K, MATSUDA C. Fatigue behaviour of Al/steel dissimilar resistance spot welds fabricated using Al−Mg interlayer [J]. Science and Technology of Welding and Joining, 2016, 21(3): 223−233.

[15] LEE Y K, JEONG H C, PARK K B, KIM Y J, CHO J H. Development of numerical analysis model for resistance spot welding of automotive steel [J]. Journal of Mechanical Science and Technology, 2017, 31(7): 3455−3464.

[16] KARATHANASOPOULOS N, MOHR D. Strength and failure of self-piercing riveted aluminum and steel sheet joints: Multi-axial experiments and modeling [J]. Journal of Advanced Joining Processes, 2022, 5: 100107.

[17] MESCHUT G, MERKLEIN M, BROSIUS A, DRUMMER D, FRATINI L, FÜSSEL U, GUDE M, HOMBERG W, MARTINS P A F, BOBBERT M. LECHNER M, KUPFER R, GRÖGER B, HAN D, KALICH J, KAPPE F, KLEFFEL T, KÖHLER D, KUBALL C M, POPP J, RÖMISCH D, TROSCHITZ J, WISCHER C, WITUSCHEK S, WOLF M. Review on mechanical joining by plastic deformation [J]. Journal of Advanced Joining Processes, 2022, 5: 100113.

[18] ZHOU Qiao-ying, YAO Zai-qi, XU Cong-chang, ZHOU Da-yong, LIU Wei-xue, LI Luo-xing. Shared mechanism between flow drill screw and friction stir welding and its impact on failure prediction of steel-aluminum joints [J]. Journal of Materials Processing Technology, 2023, 311: 117796.

[19] SELVARAJ S K, SRINIVASAN K, DESHMUKH J, AGRAWAL D, MUNGILWAR S, JAGTAP R, HU Y C. Performance comparison of advanced ceramic cladding approaches via solid-state and traditional welding processes: A Review [J]. Materials, 2020, 13(24): E5805.

[20] MENG Xiang-chen, XIE Yu-ming, SUN Shu-ming, MA Xiao-tian, WAN Long, CAO Jian, HUANG Yong-xian. Lightweight design: Friction-based welding between metal and polymer [J]. Acta Metallurgica Sinica (English Letters), 2023, 36: 881−898.

[21] NIU Si-zhe, MA Yun-wu, LOU Ming, ZHANG Chao-qun, LI Yong-bing. Joint formation mechanism and performance of resistance rivet welding (RRW) for aluminum alloy and press hardened steel [J]. Journal of Materials Processing Technology, 2020, 286: 116830.

[22] MILES M P, KOHKONEN K, PACKER S, STEEL R, SIEMSSEN B, SATO Y S. Solid state spot joining of sheet materials using consumable bit [J]. Science and Technology of Welding and Joining, 2009, 14(1): 72−77.

[23] MILES M P, FENG Z, KOHKONEN K, WEICKUM B, STEEL R, LEV L. Spot joining of AA 5754 and high strength steel sheets by consumable bit [J]. Science and Technology of Welding and Joining, 2010, 15(4): 325−330.

[24] SHAN He, MA Yun-wu, NIU Si-zhe, YANG Bing-xin, LOU Ming, LI Yong-bing, LIN Zhong-qin. Friction stir riveting (FSR) of AA6061-T6 aluminum alloy and DP600 steel [J]. Journal of Materials Processing Technology, 2021, 295: 117156.

[25] SUN Yi-ming, HUANG Rong-rong, ZHAO Hong-yun, CHEN Xi, JIANG Meng, WU Lai-jun, CHEN Bo, TAN Cai-wang. Enhancement of resistance element welding of AA6061 to DP600 steel by using external magnetic field [J]. Journal of Manufacturing Processes, 2022, 80: 347−358.

[26] RUSZKIEWICZ B J, SKOVRON J D, ABSAR S, CHOI H S, ZHAO X, MEARS L, ABKE T, IPEKBAYRAK K. Parameter sensitivity and process time reduction for friction element welding of 6061-T6 aluminum to 1500 MPa press-hardened steel [J]. SAE International Journal of Materials and Manufacturing, 2018, 12(1): 41−56.

[27] SQUIRES L, LIM Y C, MILES M P, FENG Z. Mechanical properties of dissimilar metal joints composed of DP 980 steel and AA 7075-T6 [J]. Science and Technology of Welding and Joining, 2015, 20(3): 242−248.

[28] LIU Lan-lan, LI Wen-bo, DENG Zhi-yong, XU Song, XU Yu-rong, ZENG Ling-bin, LI Deng-ke, YANG Yang, ZHONG Zhen. Effect of moisture on corrosion behavior of Q235 steel in bentonite clay [J]. International Journal of Electrochemical Science, 2023, 18(6): 100164.

[29] OU Yang-xin, DENG Yong-fang, ZHAO Yun-cai, ZENG Jin-cheng, XIAO Shun. Mechanical properties and microstructure of conical joints for dissimilar steels continuous drive friction welding [J]. Journal of Materials Engineering and Performance, 2023, 32(12): 5239−5248.

采用 1045 钢制铆钉对 AA 7075-T6 铝合金和低碳钢进行摩擦塞−铆复合点焊

刘雅佳，李建宇，谢泽豪，陈树海，杨 健，黄继华，赵志毅

北京科技大学 材料科学与工程学院，北京 100083

摘 要：采用一种基于具有尖状底端和凹槽头部形状的钢制铆钉的新型摩擦塞−铆复合点焊工艺，对 7075-T6 铝合金/低碳钢异种金属进行焊接。研究接头的宏观形貌、微观形貌、显微硬度和搭接剪切性能。随着主轴下压距离的增加，铆钉尖端与下层钢板发生摩擦焊接，形成具有冶金结合的固相焊接区。此外，接头处形成的钩子状结构为机械连接提供了可能。实验结果表明，在 3.4 mm 的主轴下压距离、4000 r/min 的主轴转速和 2.4 mm/s 的主轴下压速度的优化工艺参数组合下，接头的最大搭接剪切载荷能达到 14.36 kN，该接头在铝合金母材中发生失效。

关键词：摩擦塞−铆复合点焊；铝合金；低碳钢；异种金属连接

(Edited by Xiang-qun LI)